The Astrophysical Journal, 919:93 (8pp), 2021 October 1 https://doi.org/10.3847/1538-4357/ac11f0

Multimessenger Implications of Sub-PeV Diffuse Galactic Gamma-Ray Emission

Ke Fang[1] and Kohta Murase[2,3,4,5]
[1] Department of Physics, Wisconsin IceCube Particle Astrophysics Center, University of Wisconsin–Madison, Madison, WI 53706, USA; kefang@physics.wisc.edu
[2] Department of Physics, The Pennsylvania State University, University Park, PA 16802, USA
[3] Department of Astronomy & Astrophysics, The Pennsylvania State University, University Park, PA 16802, USA
[4] Center for Multimessenger Astrophysics, Institute for Gravitation and the Cosmos, The Pennsylvania State University, University Park, PA 16802, USA
[5] Center for Gravitational Physics, Yukawa Institute for Theoretical Physics, Kyoto, Kyoto 606-8502 Japan
Received 2021 April 19; revised 2021 June 29; accepted 2021 July 5; published 2021 September 29

Abstract

The diffuse Galactic gamma-ray flux between 0.1 and 1 PeV has recently been measured by the Tibet ASγ Collaboration. The flux and spectrum are consistent with the decay of neutral pions from hadronuclear interactions between Galactic cosmic rays and the interstellar medium (ISM). We derive the flux of the Galactic diffuse neutrino emission from the same interaction process that produces the gamma rays. Our calculation accounts for the effect of gamma-ray attenuation inside the Milky Way and uncertainties due to the spectrum and distribution of cosmic rays, gas density, and infrared emission of the ISM. We find that the contribution from the Galactic plane (GP) to the all-sky neutrino flux is $\lesssim$5%–10% around 100 TeV. The Galactic and extragalactic neutrino intensities are comparable in the GP region. Our results are consistent with the upper limit reported by the IceCube and ANTARES Collaborations, and predict that next-generation neutrino experiments may observe the Galactic component. We also show that the Tibet ASγ data imply either an additional component in the cosmic-ray nucleon spectrum or contribution from discrete sources, including PeVatrons such as superbubbles and hypernova remnants, and PeV electron accelerators. Future multimessenger observations between 1 TeV and 1 PeV are crucial to decomposing the origin of sub-PeV gamma-rays.

Unified Astronomy Thesaurus concepts: Galactic cosmic rays (567); Neutrino astronomy (1100); High-energy cosmic radiation (731)

1. Introduction

Diffuse gamma-rays with energies between 100 TeV and 1 PeV have recently been detected by the Tibet air-shower gamma (Tibet ASγ) experiment. The arrival directions of the sub-PeV gamma-rays extend over the Galactic plane (GP) and are consistent with being from diffuse cosmic rays in the Galaxy (Amenomori et al. 2021). The origin of cosmic rays has been an enigma especially around and beyond the knee energy at $E_{\rm knee} \sim 3$–4 PeV. Various sources, including superbubbles, hypernovae, supernovae in dense circumstellar material, merger remnants, pulsar wind nebulae, and the Galactic center (GC), have been proposed as potential contributors. Dissecting the diffuse gamma-ray emission at MeV–GeV energies (Hunter et al. 1997; Ackermann et al. 2012) to PeV energies is important to understanding the cosmic-ray sources and propagation physics.

Sub-PeV gamma-rays play crucial roles in multimessenger astrophysics. The detection of ∼0.1–1 PeV neutrinos enables us to probe ∼3–30 PeV protons beyond the knee energy. The IceCube experiment has measured diffuse TeV–PeV neutrinos that are consistent with an extragalactic origin (Aartsen et al. 2013a, 2013b, 2015, 2020; Stettner 2019). The neutrino and gamma-ray connection has been shown to be powerful for revealing both Galactic and extragalactic sources of neutrinos (Murase et al. 2013; Ahlers & Murase 2014; Murase et al. 2016).

To date diffuse Galactic neutrino emission has not been discovered (Aartsen et al. 2017; Albert et al. 2018), despite that it has been predicted to exist for decades (Stecker 1979; Kheirandish 2020 for a recent review) and studied in light of the IceCube measurements (Joshi et al. 2013; Ahlers & Murase 2014; Anchordoqui et al. 2014; Kachelrie & Ostapchenko 2014; Neronov et al. 2014; Spurio 2014; Gaggero et al. 2015; Palladino & Vissani 2016; Denton et al. 2017). In particular, primarily based on previous sub-PeV gamma-ray limits posed by the CASA-MIA (Borione et al. 1998) and KASCADE experiments, Ahlers & Murase (2014) showed that the Galactic contribution to IceCube neutrinos is subdominant (see also Murase et al. 2016), and the GP may give ∼3%–10% of the 10–100 TeV all-sky neutrino flux with $E_\nu^2 \Phi_\nu^{\rm IC} \sim (5\text{–}10) \times 10^{-8}$ GeV cm^{-2} s^{-1} sr^{-1} (Aartsen et al. 2015, 2020). This is also consistent with neutrino constraints (e.g., Spurio 2014; Ahlers et al. 2016) as well as the latest IceCube and ANTARES results, $\lesssim$8.5% (Albert et al. 2018).

The Galactic disk is magnetized, and can be regarded as a cosmic-ray "reservoir" with a typical escape timescale of $t_{\rm esc} \sim 30\,{\rm Myr}\,(R/1\,{\rm GV})^{-\delta}$ (e.g., Murase & Fukugita 2019), where R is the rigidity and $\delta \sim 0.3$–0.5. Pionic gamma-rays and neutrinos are coproduced when cosmic-ray ions interact with gas and dust particles in the Galaxy (Hayakawa 1952; Stecker 1977). The detection of diffuse Galactic gamma-rays therefore provides a solid reference to the flux level of the diffuse Galactic neutrinos as well as the cosmic-ray confinement and injection around the knee energy. In this work, by taking into account details of the gamma-ray attenuation along the line of sight, we evaluate the diffuse Galactic neutrino flux using the sub-PeV gamma-ray flux observed by the Tibet ASγ experiment. We show that the Galactic contribution can be comparable to the extragalactic flux in the direction to the GP, especially below $E_\nu \lesssim 100$ TeV, and may be observed by the next-generation neutrino telescopes. Our conclusion also applies to neutrino emission from unresolved sources in the Galaxy.

This paper is organized as follows. We study the diffuse neutrino emission in Section 2. We discuss the potential

contribution to sub-PeV gamma-rays from discrete sources, including Cygnus Cocoon (Section 3.1.1) and unresolved hadronic (Section 3.1.2) and leptonic (Section 3.2) sources. We conclude in Section 4.

2. Multimessenger Connection in Galactic Diffuse Emission

In hadronuclear (pp) scenarios, the differential spectrum of neutrinos and gamma rays per interaction are related by (e.g., Murase et al. 2013; Ahlers & Murase 2014),

$$E_\nu^2 \frac{dN_\nu}{dE_\nu} \approx \frac{3}{2}\left(E_\gamma^2 \frac{dN_\gamma}{dE_\gamma}\right)\Bigg|_{E_\nu \approx E_\gamma/2}, \quad (1)$$

considering that the ratio of charged and neutral pions is approximately 2:1 at high energies and each neutrino carries $\sim 1/4$ of the pion energy. Neutrinos with characteristic energy carry $\sim$3%–5% of the parent nucleon energy, i.e., $E_\nu \sim (0.03\text{–}0.05)E_p$. Equation (1) is further subject to the gamma-ray attenuation. This is because PeV gamma-rays travel only $\sim$10 kpc. In this work, we take into account the effect of the gamma-ray absorption in detail. We do not consider electromagnetic cascades since the effect is small for steep spectra with $\alpha_\nu > 2$ (see, e.g., Murase & Beacom 2012).

2.1. Methods

Below, $\boldsymbol{x}$ indicates a cylindrical coordinate system with the GC at the origin and the GP on the xy plane, referred to as the GC frame. The projected distance of $\boldsymbol{x}$ to the GC on the xy plane is noted as r and the distance to the plane is z. This coordinate system is suitable for the description of the diffuse infrared emission and cosmic-ray source distribution in the Galaxy, which are approximately cylindrically symmetric. For observation of neutrinos and gamma rays at the solar neighborhood we will use the Galactic coordinate $\boldsymbol{x}_g$. Taking the direction toward the GC as the x-axis, we have $\boldsymbol{x}_g = (s\cos b\cos l, s\cos b\sin l, s\sin b)$, where s is the distance to the observer (the Sun) and l and b are the Galactic longitude and latitude, respectively. $\boldsymbol{x}_g$ and $\boldsymbol{x}$ are converted by $\boldsymbol{x} = \boldsymbol{x}_g + \boldsymbol{x}_{\rm obs}$, where $\boldsymbol{x}_{\rm obs}$ is the coordinate of the observer in the GC frame.

The inverse of the mean free path for a gamma ray of energy E_γ and direction $\hat{u}$ at a space point $\boldsymbol{x}$ is

$$\lambda_{\gamma\gamma}^{-1}(E_\gamma, \hat{u}, \boldsymbol{x}) = \int d\Omega (1 - \hat{u}\cdot\hat{k}) \int d\varepsilon \frac{dn}{d\varepsilon d\Omega} \times (\boldsymbol{x})\sigma_{\gamma\gamma}(E_\gamma \varepsilon (1 - \hat{u}\cdot\hat{k})). \quad (2)$$

In the equation $\sigma_{\gamma\gamma}$ is the cross section for pair production $\gamma\gamma \to e^+e^-$, Here $dn/d\varepsilon d\Omega(\boldsymbol{x})$ is the number density of target photons per unit energy per unit solid angle at the position $\boldsymbol{x}$ and direction $\hat{k}$. For photons above 10 TeV, the main target photons are the cosmic microwave background (CMB) and the infrared emission by dust. The former is uniform within the Galaxy, while the latter depends on r and z. We describe the calculation of $dn/d\varepsilon d\Omega(\boldsymbol{x})$ and discuss the attenuation by different radiation fields in Appendix A.

The $\gamma\gamma$ optical depth $\tau_{\gamma\gamma}$ for a photon traveling from an initial position $\boldsymbol{x}_0$ to an observer at $\boldsymbol{x}_{\rm ob}$ is

$$\tau_{\gamma\gamma}(E_\gamma, \boldsymbol{x}_0, \boldsymbol{x}_{\rm ob}) = \int_0^{|\boldsymbol{x}_{\rm ob}-\boldsymbol{x}_0|} ds\ \lambda_{\gamma\gamma}^{-1}(E_\gamma, \hat{u}, \boldsymbol{x}_0 + s\hat{u}) \quad (3)$$

with $\hat{u} = (\boldsymbol{x}_{\rm ob} - \boldsymbol{x}_0)/|\boldsymbol{x}_{\rm ob} - \boldsymbol{x}_0|$. The probability of a photon surviving from the pair production is (Vernetto & Lipari 2016)

$$P_{\gamma,\rm surv}(E_\gamma, \boldsymbol{x}_0, \boldsymbol{x}_{\rm ob}) = \exp(-\tau_{\gamma\gamma}(E_\gamma, \boldsymbol{x}_0, \boldsymbol{x}_{\rm ob})). \quad (4)$$

The averaged gamma-ray intensity from a region of solid angle $\Delta\Omega$ is the sum of the photons that have survived from all the sources in that area:

$$E_\gamma^2 \Phi_\gamma^\Omega \approx \frac{1}{\Delta\Omega}\int d\Omega \int ds\ n_{\rm CR} n_N(\boldsymbol{x}_0)\sigma_{pp} c \times \left(E_\gamma^2 \frac{dN_\gamma}{dE_\gamma}\right)\frac{1}{4\pi|\boldsymbol{x}_0 - \boldsymbol{x}_{\rm ob}|^2} P_{\gamma,\rm surv}(E_\gamma, \boldsymbol{x}_0, \boldsymbol{x}_{\rm ob}), \quad (5)$$

where $n_{\rm CR}n_N(\boldsymbol{x}_0)$ is the product of the cosmic ray (CR) and gas/molecular densities. σ_{pp} is the inelastic pp cross section, which moderately increases from $\sim$40 mb at $E_p = 100$ TeV to $\sim$70 mb at $E_p = 10$ PeV (e.g., Tanabashi et al. 2018). This energy dependence impacts the shapes of the intrinsic gamma-ray spectrum and the neutrino spectrum in the same way.

The all-flavor neutrino flux can be computed in the same way:

$$E_\nu^2 \Phi_\nu^\Omega \approx \frac{1}{\Delta\Omega}\int d\Omega \int ds \frac{n_{\rm CR} n_N(\boldsymbol{x}_0)\sigma_{pp} c}{4\pi|\boldsymbol{x}_0 - \boldsymbol{x}_{\rm ob}|^2}\left(E_\nu^2 \frac{dN_\nu}{dE_\nu}\right). \quad (6)$$

Notice that the chance of a neutrino interaction inside the Galaxy is negligible. In other words, the survival probability of high-energy neutrinos is always 1.

Using Equation (1), we can write the neutrino intensity using the gamma-ray intensity in the Galactic coordinate:

$$E_\nu^2 \Phi_\nu^\Omega \approx \frac{3}{2}(E_\gamma^2 \Phi_\gamma^\Omega)|_{E_\gamma = 2E_\nu} \times \frac{\int ds \int \cos b\, db \int dl\ n_{\rm CR} n_N(s, b, l)}{\int ds \int \cos b\, db \int dl\ n_{\rm CR} n_N(s, b, l) P_{\gamma,\rm surv}(E_\gamma = 2E_\nu, s, b, l)} \quad (7)$$

which is improved compared to Equation (2) of Ahlers & Murase (2014).

To account for the uncertainty caused by the $n_{\rm CR}n_N$ distribution, which depends on details of the CR propagation and gas density distribution, we consider the two limits. In the first model, as in the leaky box model, cosmic rays are assumed to be uniformly distributed within the disk (which is smaller than the cosmic-ray halo):

$$n_{\rm CR} n_N(r, z) \propto \begin{cases} 1 & r < R_{\rm disk} \text{ and } |z| < z_{\rm disk} \\ 0 & \text{otherwise} \end{cases}, \quad (8)$$

with $R_{\rm disk} = 15$ kpc and $z_{\rm disk} = 0.2$ kpc (which is compatible with the scale height of H I gas). This gives a conservative estimate on the Galactic diffuse emission (see, e.g., Ahlers & Murase 2014; Ahlers et al. 2016). In the second model, we assume that it follows the spatial distribution of supernova

remnants (SNRs):

$$n_{\rm CR} n_N(r, z) \propto \left(\frac{r}{R_\odot}\right)^{\zeta} \exp\left[-\eta\left(\frac{r - R_\odot}{R_\odot}\right) - \frac{|z|}{z_g}\right]. \quad (9)$$

where $R_\odot = 8.5$ kpc is the solar distance from the GC and the following parameter values are adopted: $\zeta = 1.09$, $\eta = 3.87$ (Green 2015), and $z_g = 0.2$ kpc (Blasi & Amato 2012). This model is appropriate when we consider GP emission from a number of discrete sources. But this would give an optimistic estimate on the Galactic diffuse emission since cosmic rays diffuse out from the sources.

Finally, the total neutrino (or gamma-ray) flux from the region of interest with Ω can be derived by the flux from the observed sky region, $\Omega_{\rm obs}$, through

$$E_i^2 F_{i,\rm GP} = E_i^2 F_{i,\rm obs} \times \frac{\int ds \int^{\Omega} d\Omega\, n_{\rm CR} n_N(s, b, l) P_{i,\rm surv}(s, b, l)}{\int ds \int^{\Omega_{\rm obs}} d\Omega\, n_{\rm CR} n_N(s, b, l) P_{i,\rm surv}(s, b, l)} \quad (10)$$

$$= \frac{\Delta\Omega n_{\rm CR}^{\Omega} \tau_{pp}^{\Omega} \tilde{P}_{i,\rm surv}^{\Omega}}{\Delta\Omega_{\rm obs} n_{\rm CR}^{\Omega_{\rm obs}} \tau_{pp}^{\Omega_{\rm obs}} \tilde{P}_{i,\rm surv}^{\Omega_{\rm obs}}}, \quad (11)$$

where i indicates either ν or γ, $n_{\rm CR}^{\Omega}$ is the averaged CR density, and τ_{pp}^{Ω} is the averaged pp optical depth (Ahlers & Murase 2014).

2.2. Results

Two neutrino spectral models are used to account for the uncertainty in the cosmic-ray nucleon spectrum (see Appendix B). The gamma-ray intensity Φ_γ^{Ω} from a sky region of solid angle Ω is obtained from Equations (7), (B1), and (B2) and normalized by fitting to the Tibet ASγ data using a χ^2 statistic:

$$\chi^2 = \sum_{i,j} \frac{(\Phi_{\gamma,\rm obs}^{\Omega_j}(E_i) - \Phi_\gamma^{\Omega_j}(E_i))^2}{(\sigma_{\gamma,\rm obs}^{\Omega_j}(E_i))^2}. \quad (12)$$

In this equation, $\Phi_{\gamma,\rm obs}^{\Omega_j}(E_i)$ and $\sigma_{\gamma,\rm obs}^{\Omega_j}(E_i)$ are the observed intensity and uncertainty of diffuse gamma-rays from sky region j in energy bin i, respectively. Two sky regions are considered, namely, *region A* with $25^\circ < l < 100^\circ$ and $|b| < 5^\circ$, and *region B* with $50^\circ < l < 200^\circ$ and $|b| < 5^\circ$. In each energy bin, the upper (lower) error is used if the model is above (below) the mean of the measurement. Amenomori et al. (2021) note that 40% of events above 398 TeV in each of the two sky regions are close to the Cygnus Cocoon (see our discussion in Section 3.1.1). Therefore, our fit in the highest-energy bin uses 60% of the measured values. The fit uses six flux points from Tibet ASγ and one free parameter, the flux norm of Equation (B1) or (8), and thus has a total of 5 degrees of freedom. The resulted chi-square per degree of freedom is $\chi^2 \sim 1.6$–2.0 and $\chi^2 \sim 0.7$–1.0 for the uniform and SNR source distribution models, respectively.

The best-fit gamma-ray intensities for the two sky regions measured by Tibet ASγ are shown as colored bands in Figure 1. The boundaries of the bands are decided by the minimum and maximum values from the four cases in use,

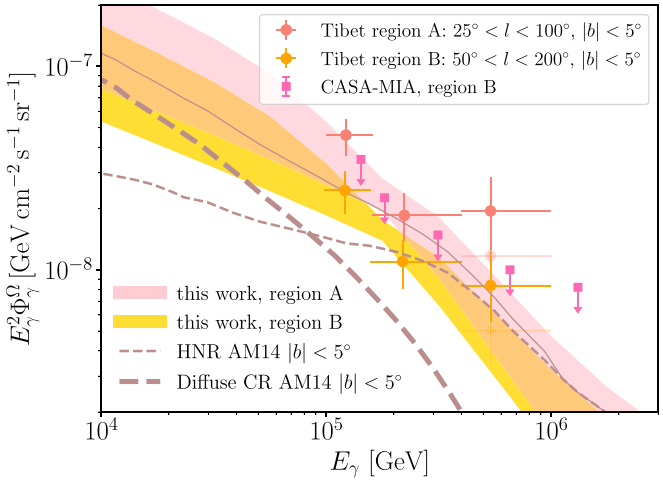

Figure 1. The diffuse Galactic gamma-ray intensity from two sky regions, region A: $25^\circ < l < 100^\circ$, $|b| < 5^\circ$, and region B: $50^\circ < l < 200^\circ$, $|b| < 5^\circ$. The red and orange data points are the Tibet ASγ measurement of the diffuse γ-ray emission from the two regions (Amenomori et al. 2021). In the last energy bin, the fainter data points indicate the residual intensity after removing events relevant to Cygnus Cocoon. The red and orange bands are the best-fit γ-ray models derived in this work, accounting for uncertainties in the gamma-ray attenuation and cosmic-ray models. The brown long and short dashed curves indicate the diffuse gamma-ray spectra for the GP and unresolved hypernova remnants, respectively, which are taken from Ahlers & Murase (2014) for $|b| < 5^\circ$. The thin solid curve shows the sum of the two components, which demonstrates that the Tibet ASγ data are also consistent with a prediction with source emission.

which include the two gamma-ray emissivity distribution models and the two cosmic-ray nucleon spectra. In particular, in these shaded bands, upper boundaries below ~150 TeV are determined by the nucleon spectrum Model A (Equation (B1)), whereas those above are governed by the nucleon spectrum Model B (Equation (B2)). See also Appendix B. We find that the sub-PeV gamma-ray spectral shape is barely affected by uncertainties in the gamma-ray attenuation. Rather, it depends on the shape of the cosmic-ray nucleon spectrum. For example, if the cosmic-ray nucleon spectrum has a break at $E_* = 0.9$ PeV (Gaisser et al. 2013), the gamma-ray spectrum should be steepened at $\sim 0.08 E_* \sim 80$ TeV, which causes a tension with the Tibet ASγ data at the highest-energy bin. The tension can readily alleviated if discrete sources make a significant contribution at sub-PeV energies as we discuss in Section 3.

Now, let us consider the GP contribution to IceCube neutrinos. Figure 2 shows the 4π-averaged intensity of diffuse Galactic neutrinos (shaded blue band) calculated using the best-fit gamma-ray models in Figure 1 and Equations (10) and (7). The GP contribution to the all-sky neutrino flux depends on neutrino energy, and is found to be $\lesssim$5%–10% in the 100 TeV range. We caution that the exact value depends on the all-sky IceCube flux and varies with energy depending on the spectra. Analytically, noting that the all-sky-averaged intensity is denoted as $\Phi_\nu \equiv (\int d\Omega\, \Phi_\nu^{\Omega}/4\pi) = (\Delta\Omega_{\rm GP}/4\pi)\Phi_\nu^{\rm GP}$, we may write

$$\frac{\Delta\Omega_{\rm GP} E_\nu^2 \Phi_\nu^{\rm GP}}{4\pi E_\nu^2 \Phi_\nu^{\rm IC}} \sim 5\% \left(\frac{E_\nu^2 \Phi_\nu^{\rm IC}}{5 \times 10^{-8}\,{\rm GeV cm^{-2}\,s^{-1}\,sr^{-1}}}\right)^{-1} \times \left(\frac{\Delta\Omega_{\rm GP}}{1.1\ {\rm sr}}\right)\left(\frac{E_\gamma^2 \Phi_\gamma^{\rm GP}|_{E_\gamma = 2E_\nu}}{2 \times 10^{-8}\,{\rm GeV cm^{-2}\,s^{-1}\,sr^{-1}}}\right). \quad (13)$$

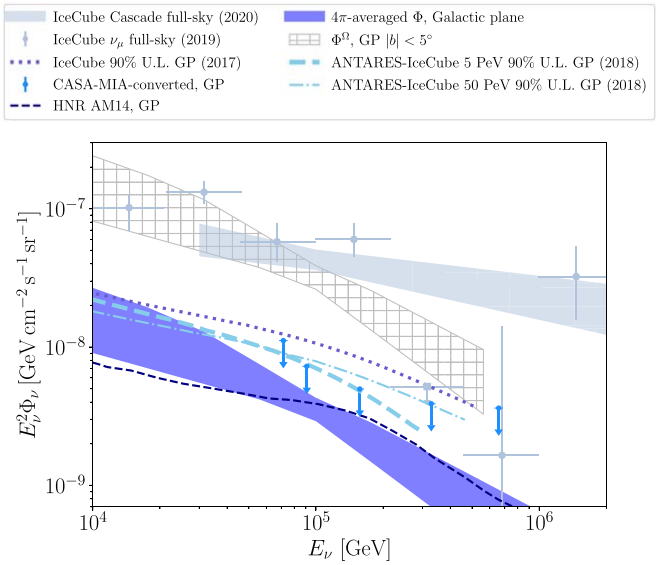

Figure 2. All-sky-averaged intensity of all flavors of diffuse neutrinos from the GP, compared to neutrino observations. The GP neutrino intensity, $E_\nu^2\Phi_\nu$, (blue shaded band) is derived with the best-fit gamma-ray intensities in Figure 1. The model is consistent with the combined upper limits at 90% confidence level posed by ANTARES and IceCube (sky-blue dashed and dashed–dotted curves; Albert et al. 2018), the 90% limits with 7 yr IceCube data (blue dotted curve; Aartsen et al. 2017), and the upper limits on neutrinos from the GP (blue downward arrows), which are derived from the CASA-MIA gamma-ray limits in region B, assuming that sources follow the SNR distribution (cyan downward arrows; Borione et al. 1998). The hatched band shows the intensity $E_\nu^2\Phi_\nu^\Omega$ of the $|b| < 5^\circ$ region, which is comparable to the isotropic neutrino background from the IceCube Cascade (light blue data points; Aartsen et al. 2020) and muon neutrino (light blue shaded area; Stettner 2019) data below ∼100 TeV.

Here the effective solid angle of the GP is assumed to be $\Delta\Omega_{\rm GP} = 2\sin b\Delta l \simeq 1.1\ {\rm sr}\ (|b|/5^\circ)(\Delta l/360^\circ)$ and $E_\gamma^2\Phi_\gamma^{\rm GP} \sim E_\gamma^2\Phi_\gamma^{\Omega_{\rm GP}}$.[6] This value is also consistent with previous results (Ahlers & Murase 2014; Ahlers et al. 2016). Following Ahlers & Murase (2014), we also show limits on GP neutrino emission by converting the CASA-MIA upper limits through Equations (7) and (10), assuming that sources follow SNR distribution. As is clearly seen in Figure 2, our results obtained with the new Tibet ASγ data are also consistent with the upper limits posed by Albert et al. (2018) and Aartsen et al. (2017) through independent neutrino observations. This is not surprising because IceCube neutrinos are consistent with an isotropic distribution, and they mostly come from the region outside the GP (Kheirandish 2020 for a review).

The hatched gray band in Figure 2 shows the neutrino intensity of the GP with $|b| < 5^\circ$. The Tibet ASγ data imply that the intensity of diffuse Galactic neutrinos can be comparable to the isotropic diffuse neutrino background in the GP region in the ∼10–100 TeV range, i.e.,

$$E_\nu^2\Phi_\nu^{\Omega_{\rm GP}} \sim E_\nu^2\Phi_\nu^{\rm IC}. \quad (14)$$

Our result suggests that the diffuse Galactic emission below ∼100 TeV can be promisingly observed by next-generation neutrino telescopes such as IceCube-Gen2 (The IceCube-Gen2 Collaboration et al. 2021), KM3Net (Adrián-Martínez et al. 2016), and Baikal-GVD (Baikal-GVD Collaboration 2018). At higher energies, the source contribution can be relevant (see the hypernova remnants curve in Figure 2 obtained by averaging the flux within $b = 10^\circ$), which is also encouraging for next-generation high-energy neutrino telescopes. Even nondetections would also be useful, because as discussed in the next section, the diffuse gamma-rays may potentially come from discrete sources.

3. Contribution of Discrete Sources to Sub-PeV Gamma-Rays and Neutrinos

The sub-PeV diffuse emission discussed in Section 2 comes from ions that were injected into the Galaxy by sources $\sim 10^4$–10^6 yr ago, which propagate in the Galactic magnetic field, and interact with gas and dust in the Milky Way. In this section we focus on the contribution of discrete sources to the sub-PeV gamma-rays observed by the Tibet ASγ experiment.

Sub-PeV gamma-rays from discrete sources are naturally expected for two main reasons. First, as noted in Section 2, a nucleon spectrum with a break energy lower than ∼1 PeV, which is suggested by the composition modeling around the knee, is in tension with the last Tibet ASγ data point. Second, theoretically, it is natural that gamma rays are produced inside or in the vicinity of PeVatrons, including the recently detected TeV source Cygnus Cocoon and other unresolved hadronic and leptonic source populations. Harder spectra of source neutrinos and gamma rays may dominate over the steep spectra of diffuse secondaries at the highest energies.

3.1. Hadronic Sources

3.1.1. Cygnus Cocoon

Amenomori et al. (2021) indicate that ∼40% of the events in their highest-energy bin are detected within 4° around the Cygnus Cocoon. Extended 1–200 TeV gamma-ray emission from the Cygnus Cocoon has recently been reported by the HAWC Observatory, with emission above 100 TeV detected at $\sim 2.4\sigma$ significance level (Abeysekara et al. 2021). The gamma-ray spectrum can be explained by protons that either have been continuously injected over the lifetime of the stellar clusters (a few Myr), or were produced by a recent (sub-Myr) burst-like event. The latter scenario invokes the presence of a PeVatron, specifically, a PeV proton accelerator with a hard spectrum $dN_p/dE_p \propto E_p^{-2.1}$.

The Cygnus OB2 association (e.g., Wright 2020) has been among the most promising sites for cosmic-ray acceleration for many years (see Bykov 2014 for a review). Superbubbles may accelerate cosmic rays up to PeV energies or beyond via multiple shocks and turbulence (Bykov & Fleishman 1992; Klepach et al. 2000). It has been shown that cosmic rays escaping from star clusters or superbubbles may explain cosmic rays above the knee energy (Murase & Fukugita 2019; Zhang et al. 2020). The Cygnus region has also been of much interest as the promising source of high-energy neutrinos (e.g., Anchordoqui et al. 2007; Beacom & Kistler 2007; Halzen & O Murchadha 2007; Halzen et al. 2017).

Figure 3 suggests that observations of the Cygnus Cocoon region above 200 TeV may disentangle the continuous and burst scenarios of Abeysekara et al. (2021). The light pink and orange data points correspond to 40% of the Tibet ASγ flux above 398 TeV from regions A and B. Since the radius of the

[6] The all-sky estimate may depend on the distribution in the vertical direction of the disk. For a a scale height of 0.1 kpc, we have $E_\gamma^2\Phi_\gamma^{\rm GP}/E_\gamma^2\Phi_\gamma^{\Omega_{\rm GP}} \simeq 1.6$ (Ahlers & Murase 2014).

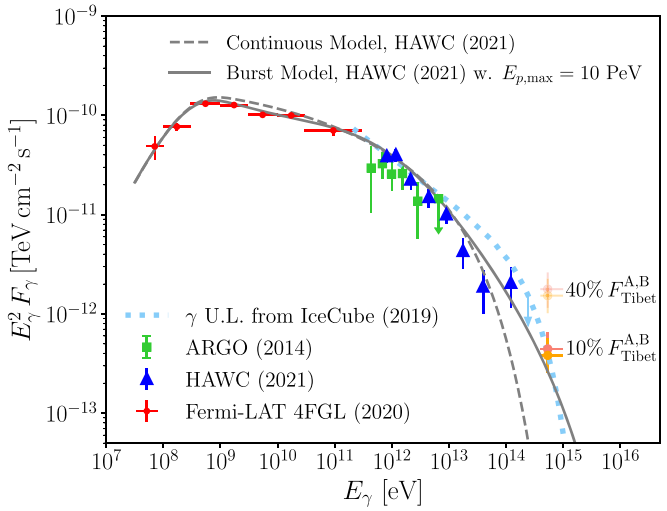

Figure 3. Spectral energy distribution of the Cygnus Cocoon measured by Fermi-LAT (Abdollahi et al. 2020), ARGO-YBJ (Bartoli et al. 2014), and HAWC (Abeysekara et al. 2021). The light pink and orange flux points indicate 40% of the Tibet ASγ flux of regions A and B (Amenomori et al. 2021). The thick pink and orange markers additionally scale the fluxes to the HAWC size of the Cygnus Cocoon. The blue dotted curve shows the limit on the γ-ray flux based on the nondetection of neutrinos from the region by IceCube (Kheirandish & Wood 2019). The two γ-ray emission models from Abeysekara et al. (2021) are shown for comparison. A significant detection of the Cygnus Cocoon at the estimated flux level may favor the burst model and the presence of a PeVatron.

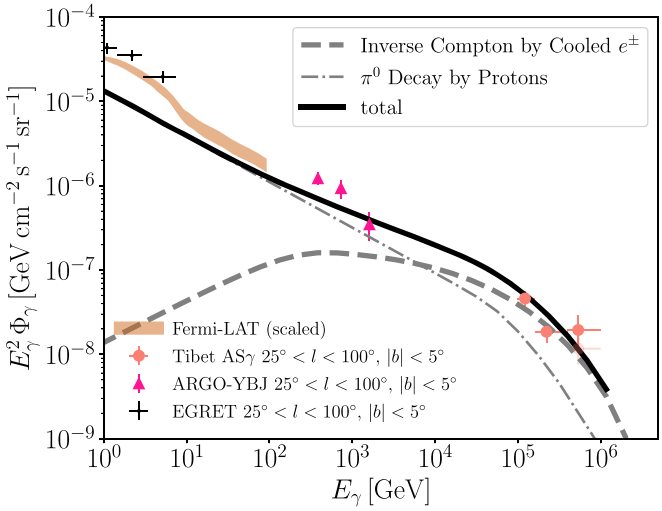

Figure 4. Demonstration of a hybrid γ-ray emission model, in which the inverse Compton of relativistic electrons (gray dashed curve) explains the Tibet ASγ measurement in the region $25° < l < 100°$ (red round data points), and π^0 decay by Galactic diffuse protons (gray dashed–dotted curve) explains the lower-energy observations of the same region by EGRET (black plus markers; Hunter et al. 1997), Fermi-LAT (brown shaded region; scaled from Ackermann et al. 2012b to the EGRET flux), and ARGO-YBJ (pink triangle data points; Bartoli et al. 2015). The electrons are assumed to have an intrinsic spectrum $dN/dE_e \propto E_e^{-2}$ and maximum energy $E_{e,\max} = 3$ PeV.

Cocoon is measured to be $\sim 2°$ at 1–100 TeV by HAWC, the thick pink and orange markers show a more conservative estimation of the Tibet ASγ flux using the average event number within the HAWC radius. We caveat that the pink and orange flux points in Figure 3 are approximate. The actual flux depends on the γ-ray morphology and the detector exposure. No high-energy neutrino emission has been detected from the Cygnus Cocoon. The blue dotted curve shows the gamma-ray upper limit converted from the IceCube limit on this source (Kheirandish & Wood 2019). For comparison, we overlay the continuous model and the burst model from Abeysekara et al. (2021). In particular, we update here the maximum proton energy in the burst model from 2 PeV to 10 PeV to accommodate the estimated Tibet ASγ flux. The other model parameters remain the same. We find that the burst scenario, hence a PeVatron, would be favored if the flux above 400 TeV reaches $\gtrsim 3 \times 10^{-13}$ TeV cm^{-2} s^{-1} assuming $\sim$30% measurement uncertainty.

3.1.2. Hypernova Remnants

Recent optical observations have revealed that energetic supernovae with a kinetic energy of $\mathcal{E}_{\rm ej} \gtrsim 10^{52}$ erg are not negligible as the cosmic-ray energy budget (e.g., Murase & Fukugita 2019), and their rate is about $\sim$3% of the core-collapse supernova rate that is $\sim$3 per century. Energetic supernovae, so-called hypernovae (that are mostly broad-line Type Ibc supernovae), and transrelativistic supernovae, which are often associated with low-luminosity gamma-ray bursts, have been widely discussed as cosmic-ray accelerators, and they may accelerate cosmic rays up to $\sim$10–100 PeV energies (e.g., Sveshnikova 2003; Murase et al. 2013; Senno et al. 2015). It has been argued that the X-ray emission from the Cygnus region can be attributed to a hypernova remnant (Kimura et al. 2013; Bluem et al. 2020). The burst model discussed in the previous subsection is consistent with such a model. The required cosmic-ray input, $\sim 10^{51}$ erg, is comparable to the energy amount of cosmic rays accelerated by a hypernova. Dozens of hypernova remnants are expected to exist in the Milky Way, and a fraction of IceCube neutrinos may come from them (Fox et al. 2013). There may be a few hypernova remnants in regions A and B, and one of them could be in the Cygnus region. As shown in Figure 1, the model (Ahlers & Murase 2014) is consistent with the Tibet ASγ data. This demonstrates the potential relevance of contributions from discrete sources, and we stress that other candidate sources are also possible.

3.2. Leptonic Sources

While the sub-PeV γ-ray emission can be plausibly explained by the decay of neutral pions from hadronuclear interactions (Amenomori et al. 2021), a leptonic origin may not yet be excluded. Figure 4 demonstrates such a scenario, where the Tibet ASγ data can in principle be explained by electrons that upscatter the CMB. We assume here that relativistic electrons are injected by discrete Galactic sources such as pulsar wind nebulae, confined close to the vicinity of the emission region, while being cooled via synchrotron radiation in the Galactic magnetic field and inverse-Compton scattering with the CMB. The steady-state electron distribution is calculated by solving the transport equation, with $B = 3$ μG and $u_{\rm CMB} = 0.26$ eV cm^{-3} for the energy density of magnetic field and the CMB. We note that B near the sources could be higher than the average interstellar medium (ISM) field strength that we take. Besides, our example model does not account for the IR radiation field at the emission sites that could further contribute to gamma-ray production below $\sim$10 TeV. At tens to hundreds of TeV electron energies the cooling timescale is much shorter than the diffusion timescale; therefore, the diffusion process is negligible for the calculation. Assuming

that $Q_e \propto E_e^{-2}$ up to a maximum energy $E_{e,\max} = 3$ PeV and source emission time $\sim$0.1 Myr (just for demonstrative purposes), we find that the total electron power $L_e = \int_{m_e c^2}^{E_{e,\max}} \sim 10^{37}\,(d/5\ \mathrm{kpc})^2\ \mathrm{erg\ s^{-1}}$ is sufficient to explain the Tibet ASγ flux, where d is the average source distance. Although the mechanism of PeV electron acceleration remains an open question, leptonic sources with such hard spectra and high $E_{e,\max}$ have been previously observed (see, e.g., HAWC Collaboration et al. 2018, 2020; Fang et al. 2020).

The Galactic diffuse emission at GeV–TeV energies is expected to be contributed by the π^0 decay of hadronic cosmic rays and the inverse-Compton emission by diffuse electrons and electrons from pulsars (Ackermann et al. 2012; Linden & Buckman 2018). The dashed–dotted curve in Figure 4 shows such a component. It shows one of our benchmark cases (cosmic-ray model I and uniform source distribution) but with 50% of the best-fit normalization.

4. Conclusions and Discussion

The flux level of Galactic neutrinos has been a mystery and remains undetected by the current-generation neutrino telescopes. Using the recently measured Galactic diffuse gamma-ray intensity, we derived the neutrino flux from the GP. We took into account uncertainties in the gamma-ray attenuation and cosmic-ray spectrum, and the all-sky-averaged neutrino intensity from the GP is estimated to be $\lesssim(3-6)\times 10^{-9}\,\mathrm{GeV\,cm^{-2}\,s^{-1}\,sr^{-1}}$ at 100 TeV. Our results are consistent with both previous gamma-ray and neutrino constraints. Our calculation relies on the simple connection between neutrinos and gamma rays produced by *pp* interactions, so the results on the sub-PeV neutrino flux are not very sensitive to the chemical composition of cosmic rays as well as details of the propagation and source distribution.

The diffuse neutrino intensity toward the GP may be comparable to the extragalactic neutrino intensity in the same sky region. Given that the GP is $\sim$10% of the sky, the detection is promising for next-generation telescopes such as KM3Net and IceCube-Gen2, which may also find a large-scale anisotropy due to the Galactic component (Becker Tjus & Merten 2020). The 7 yr all-flavor IceCube GP sensitivity around 100 TeV is $\sim 10^{-8}\,\mathrm{GeV\,cm^{-2}\,s^{-1}\,sr^{-1}}$. With a factor of $\sim$5 increase in the neutrino effective area (The IceCube-Gen2 Collaboration et al. 2021), the GP sensitivity of IceCube-Gen2 may reach $\sim 3\times 10^{-9}\,\mathrm{GeV\,cm^{-2}\,s^{-1}\,sr^{-1}}$ in 10 years, while KM3Net (Aiello et al. 2019) would reach $\sim(3\text{–}6)\times 10^{-9}\,\mathrm{GeV\,cm^{-2}\,s^{-1}\,sr^{-1}}$ at 100 TeV for the diffuse Galactic neutrino spectrum, although the detailed value depends on the spectral shape. These would be sufficient to detect the diffuse neutrino flux indicated by the lower bound of the blue shaded region in Figure 2.

The origin of neutrinos below 100 TeV has emerged as a new mystery (Aartsen et al. 2015, 2020). The measured spectral index ($\sim$2.53) is compatible with that of diffuse GP emission. With these similar indices, the Tibet ASγ data imply that the GP contribution remains $\lesssim$10% even at $\sim$10–100 energies, further supporting the manifestation of extragalactic origins (Murase et al. 2016). We do not exclude possibilities that a fraction of neutrinos come from other regions such as the Galactic halo (see Section 2 of Ahlers & Murase 2014), although the Tibet ASγ off-source data imply a Galactic halo contribution lower than $E_\nu^2\Phi_\nu \lesssim 2\times 10^{-9}\,\mathrm{GeV\,cm^{-2}\,s^{-1}\,sr^{-1}}$. Other Galactic sources, such as the Fermi bubbles, have also been constrained (Ahlers & Murase 2014; Lunardini et al. 2014; Fang et al. 2017). These are consistent with the fact there is no significant northern–southern asymmetry in the neutrino sky (Aartsen et al. 2020).

While the diffuse Galactic interpretation of the Tibet ASγ data seems the most natural, discrete sources may still significantly contribute especially at the highest energies. This is especially the case if the cosmic-ray nucleon spectrum is as steep as $E^{-2.7}$ with a break energy of $\lesssim$1 PeV. If a crucial fraction of the highest-energy events detected by the Tibet ASγ experiment is associated with the Cygnus Cocoon, the presence of an efficient PeVatron would be supported. The Tibet ASγ data can also be explained by unresolved PeVatrons such as hypernova remnants in the Cygnus region and (or) other parts of the Galaxy. Finally, the leptonic scenario is not excluded. Future multimessenger observations by not only neutrino telescopes but also near-future gamma-ray experiments such as LHAASO, ALPACA, and SWGO are necessary to discriminate between these scenarios. The spatial distribution would give us crucial information, and observations in the southern sky are relevant (Ahlers & Murase 2014; Huentemeyer et al. 2019). A few or dozens of sources are sufficient to explain the sub-PeV gamma-ray intensity, which is promising for source identification.

While preparing the manuscript, we became aware that Dzhatdoev (2021), Qiao et al. (2021), and Liu & Wang (2021) appeared on arXiv. Our work was carried out independently.

We thank Markus Ahlers, Julia Becker Tjus, Kazumasa Kawata, and Walter Winter for useful comments and communications. The work of K.F. is supported by the Office of the Vice Chancellor for Research and Graduate Education at the University of Wisconsin–Madison with funding from the Wisconsin Alumni Research Foundation. The work of K.M. is supported by NSF grant No. AST-1908689, and KAKENHI No. 20H01901 and No. 20H05852. K.F. acknowledges support from the National Science Foundation (PHY-2110821). The work of K.M. is supported by NSF Grant No. AST-1908689, 2108466, and 2108467.

Appendix A
Optical Depth for Sub-PeV Gamma-Rays

Gamma rays above a few 100 TeV mostly pair-produce with the CMB. The differential number density of the isotropic blackbody emission is

$$\left.\frac{dn}{d\varepsilon d\Omega}\right|_{\rm CMB} = \frac{2\varepsilon^2}{h^3c^3}\frac{1}{e^{\varepsilon/(k_B T_{\rm CMB})}-1}, \tag{A1}$$

where h is the Planck constant, k_B is the Boltzmann constant, and $T_{\rm CMB} = 2.73$ K is the CMB temperature.

Gamma rays between $\sim$10 TeV and $\sim$1 PeV also interact with the dust emission with wavelength $\lambda \gtrsim 50\ \mu$m. We follow Vernetto & Lipari (2016) for the calculation of the infrared density field of the Galaxy. The intensity of the infrared emission at the location $\boldsymbol{x}$ and direction $\hat{k}$ is obtained by integrating the dust emissivity along the line of sight s:

$$I_\lambda(\boldsymbol{x}) = \int_0^\infty ds\ \eta_\lambda(\boldsymbol{x}+\hat{k}s). \tag{A2}$$

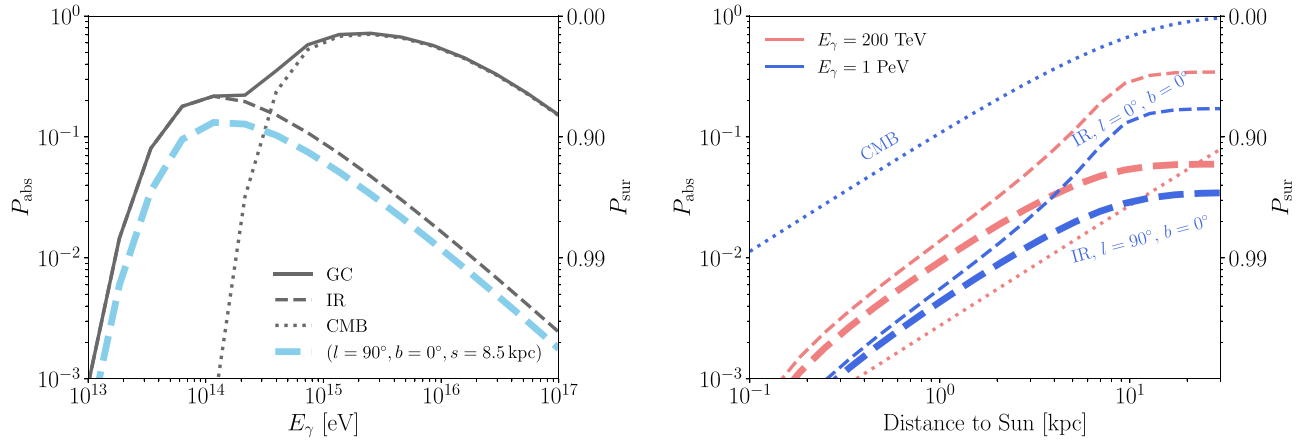

Figure 5. Survival probability of gamma rays traveling to an observer in the solar neighborhood. The attenuation due to the CMB is indicated by dotted curves and that due to the infrared dust emission is indicated by dashed curves. Left: the survival probability as a function of gamma-ray energy for photons starting from the Galactic center (GC; gray) and a certain direction ($l = 90°$, $b = 0°$, $s = 8.5$ kpc) inside the sky region where diffuse gamma-rays are observed (light blue). Right: $P_{\rm surv}$ as a function of distance to the Sun. Gamma-ray energy is indicated in color (red corresponds to $E_\gamma = 200$ TeV and blue corresponds to $E_\gamma = 1$ PeV), and the direction is indicated by the thickness of the curves (thin dashed indicates the GC direction and thick dashed indicates $l = 90°$, $b = 0°$).

Here η_λ is the power emitted per unit volume, unit solid angle and unit wavelength by the dust,

$$\eta_\lambda = \rho_d \kappa_\lambda B_\lambda(T). \tag{A3}$$

κ_λ is the absorption cross section per mass of dust, for which we have used the κ_λ values from Draine (2003) (the $R_V = 3.1$ model). $B_\lambda(T)$ is the spectral radiance of a blackbody:

$$B_\lambda(T) = \frac{2hc^2}{\lambda^5} \frac{1}{e^{hc/(\lambda k_B T)} - 1}. \tag{A4}$$

The infrared emission comes from cold and warm dust components. Their density and temperature profiles are assumed to follow the disk structure:

$$\rho_{c,w} \propto \exp\left[-\frac{r}{r^0_{c,w}} - \frac{|z|}{z^0_{c,w}}\right]. \tag{A5}$$

We adopt the $\rho^0_{c,w}$ and $T^0_{c,w}$ expressions described by Equations (16) and (17) of Vernetto & Lipari (2016). The number density of the dust emission is computed by

$$\left.\frac{dn}{d\varepsilon d\Omega}\right|_{\rm IR}(\boldsymbol{x}) = \frac{1}{c\,\varepsilon} I_\varepsilon(\boldsymbol{x}), \tag{A6}$$

where $I_\varepsilon = I_\lambda \lambda/\varepsilon$. The extragalactic background light may also interact with gamma rays. However, it is subdominant comparing to the Galactic dust emission and therefore ignored in our calculation.

Figure 5 compares the attenuation effect of CMB and infrared photons for gamma rays traveling from the different directions at various energies. Gamma rays above ∼500 TeV are mostly absorbed by the CMB. Gamma rays between ∼50 TeV and ∼500 TeV may pair-produce with the dust emission. The survival probability depends on the direction and distance of the gamma-ray source. Due to the spatial distribution of the dust, gamma rays from the inner Galaxy are more absorbed than those from the other parts of the Galaxy.

Appendix B
Diffuse Galactic Neutrino Spectrum

The cosmic-ray nucleon spectrum between 10 TeV and 10 PeV has been studied by different groups based on the measured cosmic-ray spectrum and modeling of the chemical composition (e.g., Hörandel 2003; Gaisser 2012, 2013; Thoudam et al. 2016; Lipari & Vernetto 2020). The fitting to observation relies on the assumption of the spectral model, including the dependence of the break energy on the charge and the mass number of each chemical group. It also depends on the choice of hadronic interaction models. For example, based on direct measurements of cosmic rays, Hörandel (2003) presented the polygonato model with the rigidity-dependence hypothesis, where the rigidity cutoff is set to 4 PeV (see also Gaisser 2012). However, the proton spectral break may exist well below the knee energy, and nuclei such as helium may be dominant around the knee (see also Gaisser et al. 2013; Lipari & Vernetto 2020). More recently, Lipari & Vernetto (2020) showed that different proton spectral indices are needed to explain the KASCADE (The KASCADE-Grande Collaboration et al. 2013) and IceTop/IceCube (Aartsen et al. 2019) data that are interpreted with QGSJet and Sibyll models. To account for uncertainties in the cosmic-ray spectrum and composition, we consider two models for the diffuse Galactic neutrino spectrum. In Model A, following Ahlers & Murase (2014), we adopt

$$\frac{dN}{dE_\nu} \propto E_\nu^{-\alpha_\nu}\left[1 + \left(\frac{E_\nu}{E^*}\right)^w\right]^{-\delta/w} \tag{B1}$$

with $\alpha_\nu = 2.54$, $\delta = 0.67$, $E_{\nu,*} = 0.04 \times 0.9$ PeV, and $w = 3.0$. The spectral index is based on the nucleon spectrum obtained by Gaisser (2013) with a 0.1 spectral hardening to account for the energy dependence of the inelastic pp cross section (e.g., Kamae et al. 2006; Kelner et al. 2006). The nucleon spectral cutoff, 0.9 PeV, is motivated by the limit that cosmic rays around the knee energy are dominated by helium nuclei with $A = 4$ (Gaisser 2012). The factor of ∼0.04 converts nucleon energy to neutrino energy, since leading neutrinos from pp interactions carry ∼(3–4)% of the nucleon energy in this energy range.

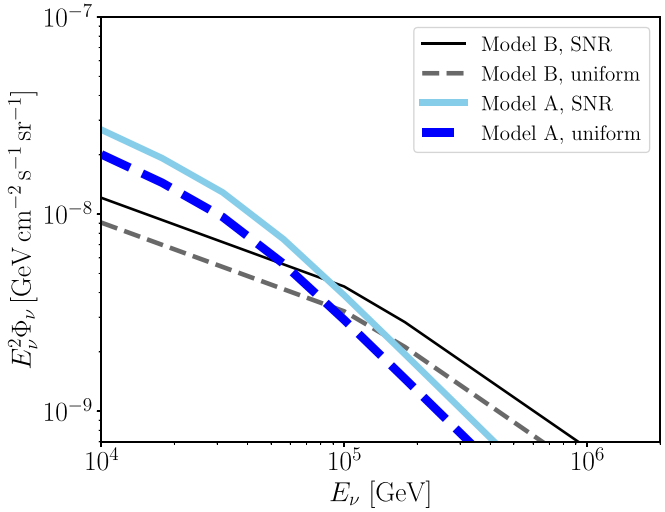

Figure 6. All-sky-averaged intensities of all-flavor diffuse neutrinos from the GP, for the two neutrino models described by Equations (B1) (Model A) and (B2) (Model B) and the two source distribution models described by Equations (8) (uniform) and (9) (SNR). The lowest and highest fluxes in each energy bin are used as the boundary of the blue filled area in Figure 2. The intensity normalization is set by the Tibet ASγ data.

In Model B, the neutrino spectrum is assumed to be a broken power law:

$$\frac{dN}{dE_\nu} \propto \begin{cases} E_\nu^{-\alpha_{\nu 1}} & E_\nu < E_{\nu,\rm bk} \\ E_\nu^{-\alpha_{\nu 2}} & E_\nu > E_{\nu,\rm bk} \end{cases}, \quad \text{(B2)}$$

where $\alpha_{\nu 1} = 2.45$, $\alpha_{\nu 2} = 2.85$, and $E_{\nu,\rm bk} = 0.04 \times 3$ PeV. This model is based on modeling of the all-particle cosmic-ray spectrum with a nucleon spectral cutoff energy of ~3–4 PeV comparable to the knee energy (e.g., Hörandel 2003; Gaisser 2012; Lipari & Vernetto 2020), but we further take possible hardening of the cosmic-ray spectral index due to the spatial inhomogeneity (by 0.15; Acero et al. 2016; Lipari & Vernetto 2018). The spectrum around the knee is believed to be largely contributed by helium nuclei, so the break energy is likely to be lower. This choice of the break energy and spectral index should be regarded as the most optimistic case. The neutrino spectra of Model A and Model B are shown in Figure 6.

ORCID iDs

Ke Fang https://orcid.org/0000-0002-5387-8138
Kohta Murase https://orcid.org/0000-0002-5358-5642

References

Aartsen, M. G., Abraham, K., Ackermann, M., et al. 2015, ApJ, 809, 98
Aartsen, M. G., Ackermann, M., Adams, J., et al. 2017, ApJ, 849, 67
Aartsen, M. G., Ackermann, M., Adams, J., et al. 2019, PhRvD, 100, 082002
Aartsen, M. G., Ackermann, M., Adams, J., et al. 2020, PhRvL, 125, 121104
Aartsen, M., Abbasi, R., Abdou, Y., et al. 2013a, PhRvL, 111, 021103
Aartsen, M., Abbasi, R., Abdou, Y., et al. 2013b, Sci, 342, 1242856
Abdollahi, S., Acero, F., Ackermann, M., et al. 2020, ApJS, 247, 33
Abeysekara, A. U., Albert, A., Alfaro, R., et al. 2021, NatAs, 5, 465
Acero, F., Ackermann, M., Ajello, M., et al. 2016, ApJS, 223, 26
Ackermann, M., Ajello, M., Atwood, W. B., et al. 2012b, ApJ, 750, 3
Adrián-Martínez, S., Ageron, M., Aharonian, F., et al. 2016, JPhG, 43, 084001
Ahlers, M., Bai, Y., Barger, V., & Lu, R. 2016, PhRvD, 93, 013009
Ahlers, M., & Murase, K. 2014, PhRv, D90, 023010
Aiello, S., Akrame, S., Ameli, F., et al. 2019, APh, 111, 100
Albert, A., André, M., Anghinolfi, M., et al. 2018, ApJL, 868, L20
Albert, A., Andre, M., Anghinolfi, M., et al. 2018, ApJL, 868, L20
Amenomori, M., Bao, Y. W., Bi, X. J., et al. 2021, PhRvL, 126, 141101
Anchordoqui, L. A., Beacom, J. F., Goldberg, H., Palomares-Ruiz, S., & Weiler, T. J. 2007, PhRvD, 75, 063001
Anchordoqui, L. A., Goldberg, H., Lynch, M. H., et al. 2014, PhRv, D89, 083003
Baikal-GVD Collaboration, Avrorin, A. D., et al. 2018, arXiv:1808.10353
Bartoli, B., Bernardini, P., Bi, X. J., et al. 2014, ApJ, 790, 152
Bartoli, B., Bernardini, P., Bi, X. J., et al. 2015, ApJ, 806, 20
Beacom, J. F., & Kistler, M. D. 2007, PhRvD, 75, 083001
Becker Tjus, J., & Merten, L. 2020, PhR, 872, 1
Blasi, P., & Amato, E. 2012, JCAP, 2012, 011
Bluem, J., Kaaret, P., Fuelberth, W., et al. 2020, ApJ, 905, 91
Borione, A., Catanese, M. A., Chantell, M. C., et al. 1998, ApJ, 493, 175
Bykov, A. M. 2014, A&ARv, 22, 77
Bykov, A. M., & Fleishman, G. D. 1992, MNRAS, 255, 269
Denton, P. B., Marfatia, D., & Weiler, T. J. 2017, JCAP, 08, 033
Draine, B. T. 2003, ARA&A, 41, 241
Dzhatdoev, T. 2021, arXiv:2104.02838
Fang, K., Charles, E., & Blandford, R. D. 2020, ApJL, 889, L5
Fang, K., Su, M., Linden, T., & Murase, K. 2017, PhRvD, 96, 123007
Fox, D., Kashiyama, K., & Mészáros, P. 2013, ApJ, 774, 74
Gaggero, D., Grasso, D., Marinelli, A., Urbano, A., & Valli, M. 2015, ApJL, 815, L25
Gaisser, T. K. 2012, APh, 35, 801
Gaisser, T. K. 2013, in ISVHECRI 2012 - XVII International Symposium on Very High Energy Cosmic Ray Interactions, Vol. 52 (Les Ulis: EDP Sciences), 09004
Gaisser, T. K., Stanev, T., & Tilav, S. 2013, FrPhy, 8, 748
Green, D. A. 2015, MNRAS, 454, 1517
Halzen, F., Kheirandish, A., & Niro, V. 2017, APh, 86, 46
Halzen, F., & O Murchadha, A. 2007, PhRvD, 76, 123003
Hayakawa, S. 1952, PThPh, 8, 571
HAWC Collaboration, Abeysekara, A. U., Albert, A., et al. 2018, Natur., 562, 82
HAWC Collaboration, Abeysekara, A. U., Albert, A., et al. 2020, PhRvL, 124, 021102
Hörandel, J. R. 2003, APh, 19, 193
Huentemeyer, P., BenZvi, S., Dingus, B., et al. 2019, BAAS, 51, 109
Hunter, S. D., Bertsch, D. L., Catelli, J. R., et al. 1997, ApJ, 481, 205
Joshi, J. C., Winter, W., & Gupta, N. 2013, MNRAS, 3414, 3419
Kachelrie, M., & Ostapchenko, S. 2014, PhRv, D90, 083002
Kamae, T., Karlsson, N., Mizuno, T., Abe, T., & Koi, T. 2006, ApJ, 647, 692
Kelner, S. R., Aharonian, F. A., & Bugayov, V. V. 2006, PhRvD, 74, 034018
Kheirandish, A. 2020, Ap&SS, 365, 108
Kheirandish, A., & Wood, J. 2019, ICRC, 36th Int. Cosmic Ray Conf. (ICRC2019), 36, 932
Kimura, M., Tsunemi, H., Tomida, H., et al. 2013, PASJ, 65, 14
Klepach, E. G., Ptuskin, V. S., & Zirakashvili, V. N. 2000, APh, 13, 161
Linden, T., & Buckman, B. J. 2018, PhRvL, 120, 121101
Lipari, P., & Vernetto, S. 2018, PhRvD, 98, 043003
Lipari, P., & Vernetto, S. 2020, APh, 120, 102441
Liu, R.-Y., & Wang, X.-Y. 2021, ApJL, 914, L7
Lunardini, C., Razzaque, S., Theodoseau, K. T., & Yang, L. 2014, PhRv, D90, 023016
Murase, K., Ahlers, M., & Lacki, B. C. 2013, PhRvD, 88, 121301 R
Murase, K., & Beacom, J. F. 2012, JCAP, 1210, 043
Murase, K., & Fukugita, M. 2019, PhRv, D99, 063012
Murase, K., Guetta, D., & Ahlers, M. 2016, PhRvL, 116, 071101
Neronov, A., Semikoz, D., & Tchernin, C. 2014, PhRvD, 89, 103002
Palladino, A., & Vissani, F. 2016, ApJ, 826, 185
Qiao, B.-Q., Liu, W., Zhao, M.-J., Bi, X.-J., & Guo, Y.-Q. 2021, arXiv:2104.03729
Senno, N., Mészáros, P., Murase, K., Baerwald, P., & Rees, M. J. 2015, ApJ, 806, 24
Spurio, M. 2014, PhRvD, 90, 103004
Stecker, F. W. 1977, ApJ, 212, 60
Stecker, F. W. 1979, ApJ, 228, 919
Stettner, J. 2019, ICRC, 36th Int. Cosmic Ray Conf. (ICRC2019), 36, 1017
Sveshnikova, L. G. 2003, A&A, 409, 799
Tanabashi, M., Hagiwara, K., Hikasa, K., et al. 2018, PhRvD, 98, 030001
The IceCube-Gen2 Collaboration, Aartsen, M. G., et al. 2021, JPhG, 48, 060501
The KASCADE-Grande Collaboration, Apel, W. D., et al. 2013, arXiv:1306.6283
Thoudam, S., Rachen, J. P., van Vliet, A., et al. 2016, A&A, 595, A33
Vernetto, S., & Lipari, P. 2016, PhRvD, 94, 063009
Wright, N. J. 2020, NewAR, 90, 101549
Zhang, Z., Murase, K., & Mészáros, P. 2020, MNRAS, 492, 2250